ACS OMEGA

Article

Cite This: *ACS Omega* 2019, 4, 14902−14912

http://pubs.acs.org/journal/acsodf

True Photoreactivity Origin of Ti^{3+}-Doped Anatase TiO_2 Crystals with Respectively Dominated Exposed {001}, {101}, and {100} Facets

Xiaogang Liu,*[,†] Guiru Du,[†] and Meng Li[‡]

[†]College of Chemistry and Chemical Engineering and [‡]Business School, Xinyang Normal University, Xinyang, Henan 464000, P. R. China

Supporting Information

ABSTRACT: Combining the advantages of reactive crystal facets and engineering defects is an encouraging way to address the inherent disadvantages of titanium dioxide (TiO_2) nanocrystals. However, revealing the true photoreactivity origin for defective TiO_2 with coexposed or predominant exposed anisotropic facets is still highly challenging. Here, the photoreactivity of TiO_2 nanocrystals with respectively predominant exposed {001}, {101}, and {100} facets before and after Ti^{3+} doping under both ultraviolet and visible light was compared systematically. In detail, the photocatalytic H_2 production for R-TiO_2-001, R-TiO_2-101, and R-TiO_2-100 increased by a factor of 1.34, 2.65, and 3.39 under UV light and a factor of 8.90, 13.47, and 8.72 under visible light. By contrast, the photocatalytic degradation of methyl orange for R-TiO_2-001, R-TiO_2-101, and R-TiO_2-100 increased by a factor of 3.18, 1.42, and 2.17 under UV light and a factor of 4.03, 2.85, and 1.58 under visible light, respectively. The true photocatalytic activity origin for the obtained photoreduction and photo-oxidation ability is attributed to the exposure of more active sites (under-coordinated 5-fold Ti atoms), the facilitated charge transfer among {001}, {101}, and {100} facets, and the Ti^{3+} energy state with variable doping levels to extend the visible light response. This work hopefully provides significant insights into the photoreactivity origin of defective TiO_2 nanocrystals with anisotropic exposed facets.

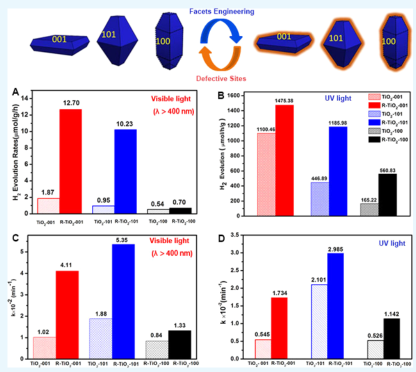

INTRODUCTION

TiO_2 has been the most intensively investigated semiconductor during the past few decades in the fields of photoelectrochemical cell,[1] photocatalysis,[2−4] solar cells,[5] sensors,[6,7] biomedical treatments,[8,9] and so on. It is highly demonstrated that the photoelectrochemical properties of TiO_2 are strongly dependent on the spatial configuration, coordination, and structural state of surface atoms, which is directly related to the exhibition on facets with different surface structures and atomic configurations.[10] Thus, facet engineering of TiO_2 has attracted great research interest in the past decade.[11−13] According to the Wulff construction model,[11] the predicted equilibrium shape of an anatase is a slightly truncated bipyramid enclosed by more than 94% {101} and fewer 6% {001} facets. The most stable {101} facet has 50% 6-fold coordinated Ti (Ti_{6c}) and 50% 5-fold coordinated Ti (Ti_{5c}) atoms, while {001} facet contains 100% Ti_{5c} atoms. The breakthrough in synthesizing micrometer-sized TiO_2 with 47% {001} and 53% {101} facets by Yang et al.[14] ignited diamond fever in terms of the surface structure and chemistry of anatase {001} and {101} facets. Other important low-index facets, such as the {100} facet,[15−17] which also have 100% Ti_{5c} atoms, may dominate when the truncated tetragonal bipyramid is elongated, as predicted by Barnard and Curtiss.[18]

Although great progress has been made to possibly verify the facets related properties of TiO_2 crystals, the true origins of facet-dependent performance have rarely been demonstrated. Although high-performance TiO_2 materials can be finely tuned through their surface and interface properties, some vital issues still need to be carefully considered in the near future research. For example, the generality of facet-dependent properties for a wide range of facets with different materials and the evaluation criteria toward the influence of surface reconstruction on the performance of micro- or nanosized facets. Typically, Pan et al.[19] prepared microsized TiO_2 single crystals with predominant {001}, {101}, and {010} facets to compare their facet-dependent photoreactivity. Unexpectedly, they found that clean anatase {101} facets exhibit higher photoreactivity than that of {001} facets. By contrast, {010} facets showed the highest photocatalytic reactivity in generating OH radicals and hydrogen evolution. Moreover, they attributed the photocatalytic performance of faceted TiO_2 to the band gap difference (T010 > T101 > T001, established by ultraviolet−visible spectra and X-ray photoelectron spectroscopy (XPS)). However, the influence of crystal size on the band gap of TiO_2 and the transfer and separation of charge carriers among different facets were neglected in their work. In addition, Zhao et al.[20] theoretically gave the following order of the work function values: {101} > {010} > {001}. Moreover, the difference of preparation method and post-treatment may also

Received: June 5, 2019
Accepted: August 12, 2019
Published: September 5, 2019

DOI: 10.1021/acsomega.9b01648
ACS Omega 2019, 4, 14902−14912

have a great influence on the photocatalytic activity of the crystal surface.

Despite the great superiority of tailored faceted TiO_2, however, facets unilaterally cannot overcome all of the inherent shortages, such as the weak visible light absorption and poor conductivity. Thus, further modifications are indispensable to enhance the photoreactivity of faceted TiO_2 crystals. Among the variable modification and regulation methods, reduced TiO_2,[21−2521−25] which contains Ti^{3+} species or oxygen vacancy, has been considered to enhance visible light absorption and possess great potential in photocatalysis, lithium-ion batteries, supercapacitors, fuel cells, and photoelectrochemical sensors. Although Ti^{3+}-doped TiO_2 exhibits stronger visible light absorption, their visible light-induced photocatalytic are still far from satisfactory. Besides, theoretical calculations have shown that too high vacancy concentration could induce a defective level below the conduction band, which may act as new capture centers for charge carriers.[26−28] Therefore, these results demonstrate that Ti^{3+} doping may provide plenty of room for preparing visible light-responding highly active TiO_2 photocatalysts. However, the underlying mechanism and effects of Ti^{3+} in affecting the photocatalytic performance of TiO_2 are still under debate.

For crystalline TiO_2, the photoreactivity is closely related to the orientation of specific exposed facets as well as their electronic structure in the surface and bulk. Thus, designing Ti^{3+} doping with highly reactive facets is used as a common strategy to optimize the photoreactivity of TiO_2. For example, Cai et al.[29] prepared Ti^{3+}-doped TiO_2 nanosheets with 26.4% of {001} facets, which exhibited enhanced photocatalytic degradation efficiency of rhodamine-B compared with that of nondoped ones. Li et al.[30] prepared oxygen-deficient blue TiO_2 nanocrystals with coexposed {101}−{001} facets to enhance the performance of visible light-induced CO_2 photoreduction. Notably, our previous works have also highlighted the pivotal role of defects in promoting the separation and transport of charge carriers and enhancing the photocatalytic activity of faceted TiO_2. However, the defective TiO_2 reported in the literature until now is usually dominated by {101} or coexposed {001}−{101} facets. So far, little attention has been focused on the engineering defects in TiO_2 nanocrystals with respectively dominated {001}, {101}, and {100} facets. Moreover, the true origin of enhanced photoreactivity of faceted TiO_2 crystals with various defective sites should be explored in detail and systematically.

Herein, to fully use the advantages of specified exposed facets and defect effects, we have prepared Ti^{3+} self-doped anatase TiO_2 nanocrystals with respectively dominated exposed {001}, {101}, and {100} facets with a facile hydrothermal reaction followed by a molten aluminum (Al) reduction method. The relationship of the exposed facets, morphologies, and defects with the photocatalytic degradation efficiency of methyl orange (MO), phenol, and H_2 production under both ultraviolet and visible light range is carefully revealed. The energy band structure and lifetime of charge carriers was further established to explore the roles of exposed reactive facets and defect sites on the photocatalytic activities.

■ RESULTS AND DISCUSSION

The crystallization phase of all of the as-prepared samples was identified by X-ray diffraction (XRD). As shown in Figure 1, all of the TiO_2 samples before and after Ti^{3+} doping present strong diffraction peaks of anatase on the basis of the JCPDS Card No. 21-1272. No other diffraction peaks were observed, indicating that the TiO_2 obtained was of good purity.

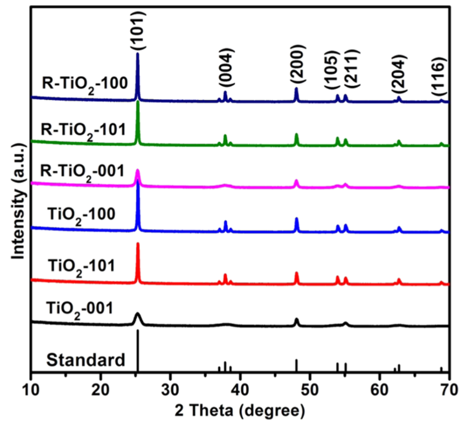

Figure 1. XRD patterns of prepared TiO_2 samples.

The morphology of the TiO_2 samples after Al reduction was observed by scanning electron microscopy (SEM) and transmission electron microscopy (TEM), the images are shown in Figure 2. SEM (Figure 2A) and TEM (Figure 2D) analysis showed that the R-TiO_2-001 sample consisted of well-defined sheet-shaped structures with a rectangular outline, a side length of ∼130 nm, and a thickness of ∼8 nm. The high-resolution TEM (HRTEM) image (inset of Figure 2D) clearly showed that the lattice spacing parallel to the top and bottom facets was ∼0.235 nm, corresponding to the (001) planes of anatase TiO_2. Based on the above structural information, the calculated percentage of the (001) facets was about 82%. As shown in the SEM images of Figure 2B, R-TiO_2-101 shows truncated bipyramidal morphology with the top and bottom surfaces being found to be high-energy {001} facets, and side surfaces remained {101} facets according to the literature.[31] As shown in the insert HRTEM images of Figure 2E, the lattice fringe with the spacing of 0.34 nm corresponded to the {101} planes of anatase further indicating that the prepared samples are truncated tetragonal bipyramids, which are enclosed by two {001} facets and eight {101} facets. As for R-TiO_2-100 shown in Figure 2C, all of the particles had well-defined lateral facets with sharp edges, and the adjacent facets were perpendicular as well as with the same width, which matches well with the equilibrium crystal shape of tetragonal faceted-nanorods with four well lateral {100} facets (shown in the insert model of Figure 2C). Furthermore, HRTEM images taken from Figure 2F indicate that three sets of clear lattice fringes with the spacings of 0.35, 0.35, and 0.48 nm can be observed, which are attributed to the corresponding (101), $(10\bar{1})$, and (002) planes of the anatase phase, respectively. Based on SEM and HRTEM images, it can be concluded that the prepared R-TiO_2-100 sample has a single-crystalline structure of the anatase phase with a growth direction along the [001] zone axis, which means that the exposed lateral facets of the as-prepared R-TiO_2-100 are mainly the {100} facets. Accordingly, the exposed facet percentages of prepared TiO_2 nanocrystals are calculated and summarized in Table S1, according to the SEM and TEM analysis as well as the equilibrium crystal shape of anatase. To clearly observe the distinction in morphology between TiO_2 samples before and after Al reduction, the SEM images of TiO_2 with dominant {001}, {101}, and {100} facets before Al reduction are also presented, as shown in Figure S1A, S1B, and S1C, respectively. Typically nanosheets, truncated

DOI: 10.1021/acsomega.9b01648
ACS Omega 2019, 4, 14902−14912

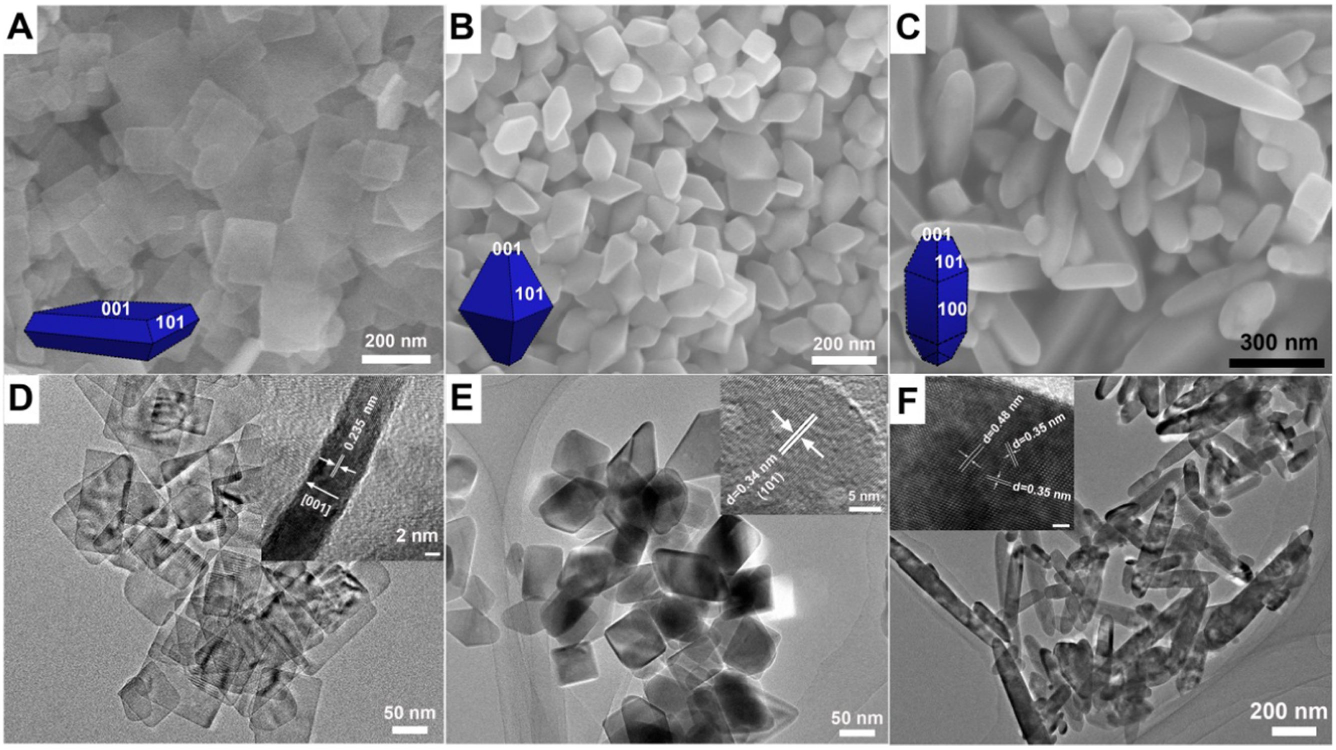

Figure 2. SEM images of (A) R-TiO_2-001, (B) R-TiO_2-101, and (C) R-TiO_2-100. TEM images of (D) R-TiO_2-001, (E) R-TiO_2-101, and (C) R-TiO_2-100; insert figures of figure (A), (B), and (C) is the corresponding equilibrium crystal shape with predominated {001}, {101}, and {100} facets. Insert figures of figure (D), (E), and (F) is their corresponding HRTEM images.

bipyramids, and tetragonal faceted-nanorod-shaped crystals can also be clearly observed, indicating that the effect of Al on the morphology of the as-prepared TiO_2 samples is negligible.

XPS analysis was performed to explore the surface states of prepared TiO_2 samples. As shown in Figure S2, XPS spectra of Ti 2p for TiO_2 samples before Ti^{3+} doping exhibit two typical peaks, which are ascribed to the Ti^{4+} states of TiO_2. Specifically, the Ti $2p_{3/2}$ and Ti $2p_{1/2}$ of TiO_2-001 peaks at 458.87 and 464.63 eV, respectively, are ascribed to typical Ti^{4+}−O bonds. As for TiO_2-101 and TiO_2-100 samples, the corresponding peaks are centered at 458.71 eV (Ti $2p_{3/2}$) and 464.39 eV (Ti $2p_{1/2}$) for TiO_2-101, while the peaks are centered at 458.69 eV (Ti $2p_{3/2}$) and 458.87 eV (Ti $2p_{1/2}$) for TiO_2-100 samples. It is reasonable for this discrepancy of binding energy since each dominant facet of the as-prepared TiO_2 samples possesses the different atomic arrangements and configurations[32,33] (i.e., the {001}, {101}, and {100} facets have 100, 50, and 100% five-coordinate Ti (Ti_{5c}) atoms, as shown in Figure S3A−C, respectively), the surface electronic structures are therefore different. As for Ti^{3+}-doped TiO_2, the corresponding XPS spectra of Ti 2p are identical to that of nonreduced ones after carefully comparing with the original ones, which is mainly due to the relatively lower contents of Ti^{3+} species. To quantitatively evaluate the contents of Ti^{3+} and better understand the correlation of Ti^{3+} with the exposed facets, a Gauss fitting of Ti 2p peaks was thus established to evaluate the Ti^{3+}/Ti^{4+} fraction (i.e., peak areas ratio of Ti^{3+}/Ti^{4+}), as shown in Figure 3. Notably, it can be seen that small shoulders at 457.9 and 463.6 eV were observed, which is ascribed to the characteristic feature of Ti^{3+} species.[34,35] Moreover, the obtained Ti^{3+}/Ti^{4+} ratio in the three TiO_{2-x} samples is on the order of R-TiO_2-001 (0.058) > R-TiO_2-101 (0.048) > R-TiO_2-100 (0.032). The obtained XPS fitting result is in good agreement with ESR analysis and digital photography of the prepared TiO_2 samples. Besides, the XPS spectra of F 1s for TiO_2-001 and R-TiO_2-001 samples are also examined, as shown in Figure S4. The results indicate that the fluorine species on the surface of TiO_2 can be easily removed under both air and aluminum atmosphere at 500 °C in our experiment. Besides, no XPS signal of Al element was observed for the Ti^{3+}-doped TiO_2 (Figure S5A,B).

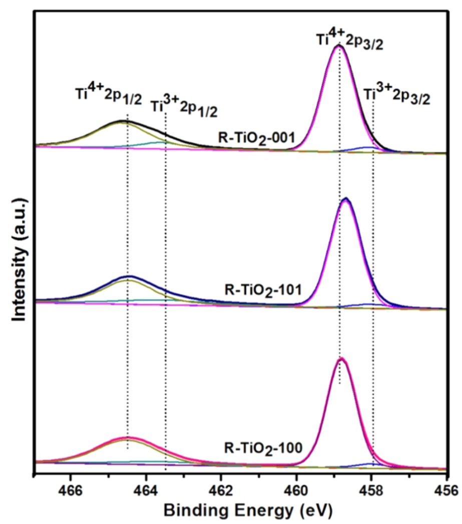

Figure 3. XPS spectra of Ti 2p for TiO_2 with different predominated exposed facets after Ti^{3+} doping.

To further characterize the effects of Al atmosphere treatment and detect the Ti^{3+} species, electron paramagnetic resonance (EPR) measurement was conducted, as shown in Figure 4. For pristine TiO_2 with different dominant facets, a

DOI: 10.1021/acsomega.9b01648
ACS Omega 2019, 4, 14902−14912

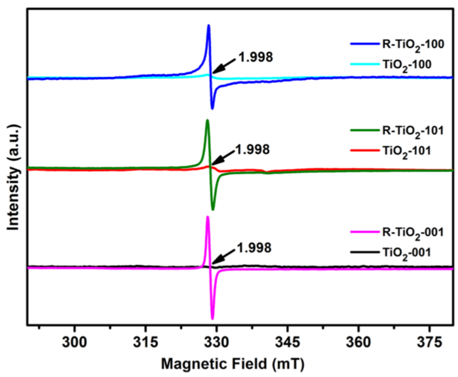

Figure 4. EPR spectra of TiO_2 with predominated exposed {001}, {101}, and {100} facets before and after Al reduction.

relatively weak paramagnetic peak at a g-factor of 1.998 indicates the presence of Ti^{3+} in the bulk,[36−38] while for R-TiO_2-001, R-TiO_2-101, and R-TiO_2-100, a stronger and sharper peak appears at the same position, suggesting that a large amount of Ti^{3+} species in bulk was introduced by Al atmosphere treatment. It is reported that the shape of the surface Ti^{3+} signal is usually broad, but bulk Ti^{3+} has a narrow axially symmetric signal.[39] In addition, it is considered that surface Ti^{3+} and subsurface Ti^{3+} showed dominant sharp signals at g = 1.918 and 1.945, respectively.[30,40] Furthermore, the relative intensity of the characteristic Ti^{3+} peak for each Al reduced TiO_2 with dominant facets was precisely examined, and the characteristic intensity ratio of R-TiO_2-100/R-TiO_2-101/R-TiO_2-001 is 0.26:0.96:1, implying that the concentration of Ti^{3+} for the reduced TiO_2 is also different.

Furthermore, the colors of the as-reduced TiO_2 samples further confirm the existence of Ti^{3+} compared with that of nonreduced ones, as shown by their digital photograph presented in Figure S6. Interestingly, we also found that although the TiO_2 with different dominant facets were processed in Al atmosphere at the same temperature of 800 °C, the color of the reduced TiO_2 was rather different, showing black (R-TiO_2-001), dark gray (R-TiO_2-100), and light gray (R-TiO_2-101), respectively. This indicates that the exposed facets may have a certain influence on the doping concentration of Ti^{3+}. Moreover, UV−visible absorption spectra are also provided, as shown in Figure 5A. The spectrum of Ti^{3+}-doped samples shifts to a longer wavelength revealing a decrease in the band gap. Meanwhile, the absorbance in the visible range is strongly enhanced compared to the unreduced ones. In addition, the absorption intensity in the visible light range differs among the Ti^{3+}-doped anatase TiO_2 and shows an order of R-TiO_2-101 > R-TiO_2-100 > R-TiO_2-001. The Kubelka−Munk function is used to calculate the band gap energy of the prepared TiO_2, as shown in Figure 5B. The band gap of TiO_2 before reduction is estimated as 3.07 eV (TiO_2-001), 3.13 eV (TiO_2-101), and 3.09 eV (TiO_2-100), while all of the values decreased with varying degrees to 2.94 eV (R-TiO_2-001), 2.63 eV (R-TiO_2-101), and 2.69 eV (R-TiO_2-100).

Moreover, the pore structure-related properties were investigated, as shown in Figure S7. All of the curves can be classified as type IV isotherms (Figure S7A) with the presence of a hysteresis loop in the relative pressure of 0.7−1.0. The adsorption/desorption isotherms of the sample before and after Al reduction is about the same, indicating that the Al reduction process has little effect on the porosity of the prepared TiO_2 samples. The hysteresis loop of TiO_2-001 and R-TiO_2-001 moved to a lower pressure zone compared with that of the other four samples, indicating that the specific surface area and pore size of the sample were relatively smaller. As can be seen from Figure S7B, all of the prepared samples exhibited typical mesoporous structures. The pore-size distribution of TiO_2-001 and R-TiO_2-001 samples is wide, which may be due to the agglomeration phenomenon caused by the orientation attachment phenomenon among the {001} facets of TiO_2-001. Table S2 lists the specific surface area and pore structure parameters of the sample. It can be seen that the Brunauer−Emmett−Teller (BET)-specific surface area of R-TiO_2-001, R-TiO_2-101, and R-TiO_2-100 is 21.7914, 24.3378, and 99.5281, which shows a slightly decreased tendency relative to that of nonreduced TiO_2-001, TiO_2-101, and TiO_2-100 with the BET-specific surface area of 25.1059, 31.7491, and 103.7212, respectively. This is possibly due to the tendency of agglomeration during the calcination treatment in Al atmosphere.

The photocatalytic hydrogen production performance was evaluated, as shown in Figure 6. As shown in Figure 6A, the pristine TiO_2 with different exposed dominant facets produce different amounts of traced H_2, exhibiting an order of total hydrogen production during 5 h under ultraviolet (UV) light with TiO_2-001 > TiO_2-101 > TiO_2-100. In contrast, all of the

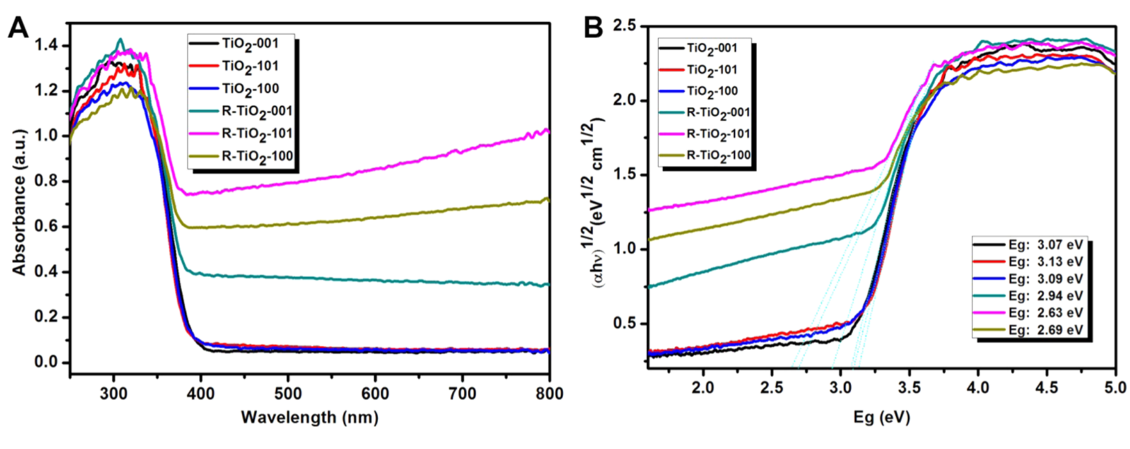

Figure 5. UV−vis diffuse reflectance spectra (A) and curves of the Kubelka−Munk function plotted against the photon energy (B) for the prepared TiO_2 samples.

DOI: 10.1021/acsomega.9b01648
ACS Omega 2019, 4, 14902−14912

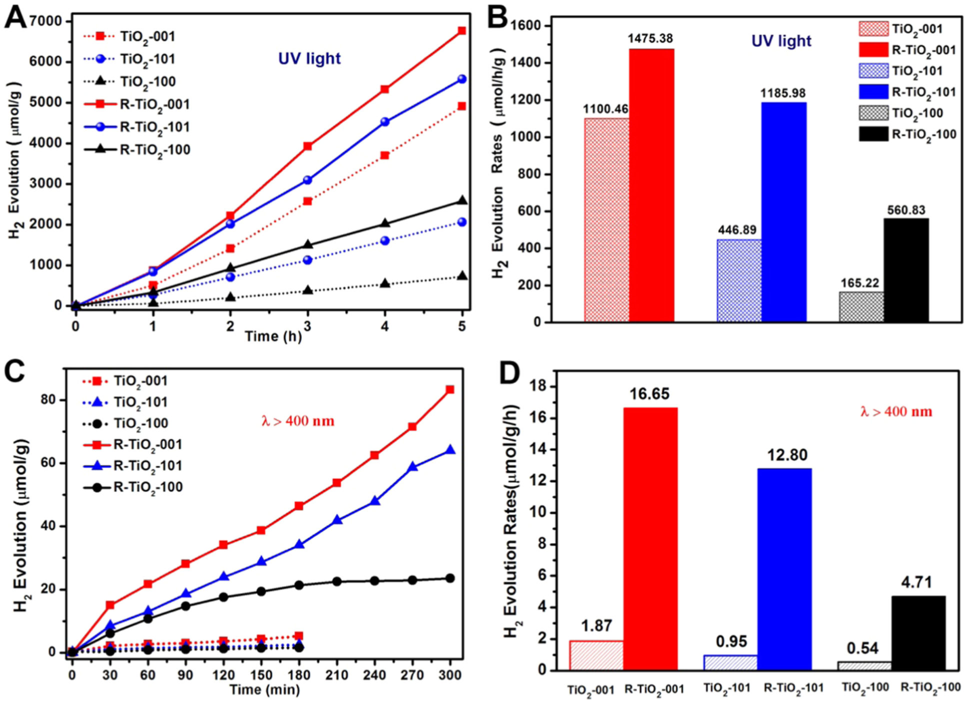

Figure 6. Time course of evolved H_2 under ultraviolet (UV) light (A) and visible light (>400 nm) irradiation (C) and the corresponding H_2 evolution rates under UV light (B) and visible light (D) for TiO_2 nanocrystal samples before and after Al reduction.

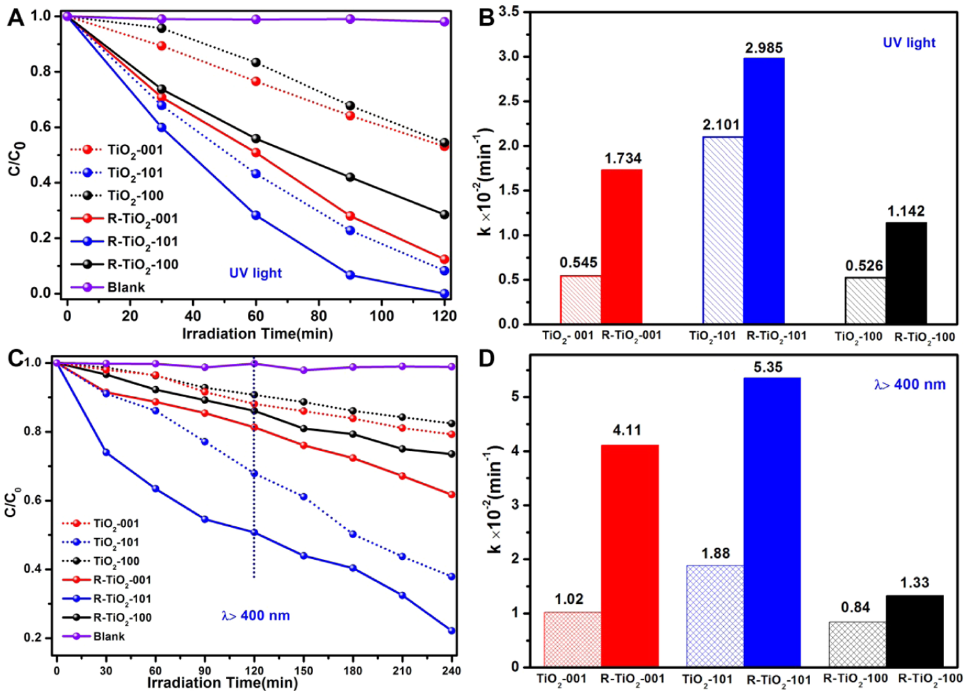

Figure 7. UV light (A) and visible light (C)-induced photocatalytic degradation of methylene orange (MO); and the corresponding pseudo-first-order kinetic rate constants under UV light (B) and visible light (D).

reduced TiO_2 samples with dominant exposed facets exhibit enhanced photocatalytic H_2 production compared with that of nonreduced ones, implying the Ti^{3+} doping does enhance the photocatalytic H_2 production performance. Furthermore, UV light-induced hydrogen production rates of the prepared TiO_2 samples is also systematically studied, as shown in Figure 6B.

More specifically, the order of the calculated hydrogen production rates of the samples before and after reduction under UV light are: 1475.38 μmol/(g h) (R-TiO_2-001), 1185.98 μmol/(g h) (R-TiO_2-101), 560.83 μmol/(g h) (R-TiO_2-100), 1100.46 μmol/(g h) (TiO_2-001), 446.89 μmol/(g h) (TiO_2-101), and 165.22 μmol/(g h) (TiO_2-100). It should be noted that though R-TiO_2-001 showed the highest photocatalytic hydrogen production rate, its hydrogen production rate was only 1.34 times that of the unreduced sample. In contrast, the hydrogen production rates of R-TiO_2-

DOI: 10.1021/acsomega.9b01648
ACS Omega 2019, 4, 14902−14912

Table 1. Comparison of Photocatalytic Performance for the As-prepared TiO_2 Samples under UV and Visible Light[a,b,c,d]

	UV light				visible light			
samples	k (10^{-2} × min^{-1})	I_k	R_H (μmol/(g h))	I_H	k' (10^{-2} × min^{-1})	I'_k	R'_H (μmol/(g h))	I'_H
TiO_2-001	0.545	3.18	1100.46	1.34	1.02	4.03	1.87	8.90
R-TiO_2-001	1.734		1475.38		4.11		16.65	
TiO_2-101	2.101	1.42	446.89	2.65	1.88	2.85	0.95	13.47
R-TiO_2-101	2.985		1185.98		5.35		12.80	
TiO_2-100	0.526	2.17	165.22	3.39	0.84	1.58	0.54	8.72
R-TiO_2-100	1.142		560.83		1.33		4.71	

[a]k and k' is the apparent rate constant of MO degradation under UV and visible light irradiation. [b]I_k and I'_k is the k and k' value ratio of TiO_2 after and before Ti^{3+} doping under UV and visible light irradiation, respectively. [c]R_H and R'_H is the hydrogen evolution rates for the as-prepared TiO_2 samples under UV and visible light irradiation, respectively. [d]I_H and I'_H is the hydrogen evolution rate ratio of TiO_2 after and before Ti^{3+} doping under UV and visible light irradiation, respectively.

101 and R-TiO_2-100 samples were far exceeding that of unreduced ones by an increasing factor of 2.54 and 3.39, respectively. In addition, Ti^{3+} doping does not affect the order of photoreduction ability of different predominant crystal facets, and the order of photocatalytic hydrogen production rate before and after Al reduction still remains: {001} > {101} > {100}. In the case of TiO_2 with different dominant facets before Al reduction under visible light irradiation, only a small amount of hydrogen can be traced (shown in Figure 6C), indicating that facets solely cannot overcome all of the deficiencies of TiO_2 especially the weak visible light absorption and its corresponding photoreactivity under visible light. However, after Ti^{3+} doping, the H_2 production rates are tremendously improved as shown in Figure 6D. To be more specific, the H_2 production rates under visible light irradiation for TiO_2-001, TiO_2-101, and TiO_2-100 is 1.87, 0.95, and 0.54 μmol/(g h) while the values of their Ti^{3+}-doped counterparts are 16.65, 12.80, and 4.71 μmol/(g h), respectively. Here, it should be emphasized that although the photocatalytic hydrogen production performance of TiO_2 samples after Ti^{3+} doping is greatly enhanced under visible light irradiation, the growth rates of H_2 production for each TiO_2 with dominant exposed facets are distinctly different. To be specific, compared with the H_2 production rates of undoped TiO_2 under visible light, the corresponding values are increased by a factor of 8.90, 13.47, and 8.72 for R-TiO_2-001, R-TiO_2-101, and R-TiO_2-100, respectively. It is reported that the defective Ti^{3+} doping level below the conduction band minimum of TiO_2 is much lower than the redox potential for H_2 evolution. Moreover, electron mobility in the bulk region is relatively lower due to this localization. Above are the two main reasons to render the photocatalytic activity of the Ti^{3+}doped TiO_2 negligible.[28,38,41]

Moreover, the degradation efficiency of MO under UV and visible light (λ > 400 nm) irradiation was analyzed (see Figure 7). As shown in Figure 7A, no significant removal of MO was detected in the absence of the catalyst under UV light irradiation. All of the Ti^{3+}-doped TiO_2 samples show enhanced MO degradation rates (C/C_0) compared with that of undoped ones after being irradiated under UV light for 2 h. Among them, TiO_2 with dominant {101} facets exhibits the most excellent photocatalytic degradation performance and almost 100 and 90% of MO was photocatalytically removed by R-TiO_2-101 and TiO_2-101 after 2 h, respectively. Moreover, the corresponding pseudo-first-order kinetics rate constant under UV light was also examined, as shown in Figure 7B. The reduced TiO_2 samples exhibit higher apparent kinetic rate constants of 1.734 × 10^{-2} min^{-1} (R-TiO_2-001), 2.985 × 10^{-2} min^{-1} (R-TiO_2-101), and 1.142 × 10^{-2} min^{-1} (R-TiO_2-100), while the undoped ones show lower kinetic constants of 0.545 × 10^{-2} min^{-1} (TiO_2-001), 2.101 × 10^{-2} min^{-1} (TiO_2-101), and 0.526 × 10^{-2} min^{-1} (TiO_2-100). More specifically, the kinetic constants of R-TiO_2-001, R-TiO_2-101, and R-TiO_2-100 increased by a factor of 3.18, 1.42, and 2.17 compared with that of TiO_2-001, TiO_2-101, and TiO_2-100, respectively. Visible light-induced photocatalytic degradation of MO was also examined, as shown in Figure 7C. Although Ti^{3+}-doped TiO_2 exhibits enhanced photocatalytic degradation of MO under visible light, the degradation rates ($1 - C/C_0$) of MO after 2 h is dramatically reduced to 50% for R-TiO_2-101 compared with that value of 100% under UV light irradiation. Given a prolonged illumination time of 5 h, the obtained degradation rates ($1 - C/C_0$) for R-TiO_2-101, R-TiO_2-001, and R-TiO_2-100 is 0.78, 0.38, and 0.26, respectively. Furthermore, R-TiO_2-001, R-TiO_2-101, and R-TiO_2-100 exhibit enhanced kinetic constants of 4.11, 5.35, and 1.33 × 10^{-2} min^{-1} under visible light irradiation, increasing by a factor of 4.03, 2.84, and 1.58 compared with that of TiO_2-001, TiO_2-101, and TiO_2-100, respectively (Figure 7D). Moreover, the photocatalytic degradation of colorless phenol under UV light has also been examined, as shown in Figure S8. Notably, the reduced TiO_2 samples still exhibit the higher photocatalytic degradation activity of phenol than the pristine ones, which is consistent with the experimental results of MO degradation. To obtain a more clear overview of photocatalytic changes of the prepared TiO_2 samples, a comparative photocatalytic activity under different light sources is summarized in Table 1.

To explore the Ti^{3+}/Pt coupling or Pt location difference in facet dominated TiO_2, the Pt particles were deposited on reduced faceted TiO_2 with different predominant exposed facets by UV-irradiation-induced photoreduction methods, the corresponding TEM images are shown in Figure 8. As can be seen clearly from Figure 8A,B, Pt nanoparticles were uniformly dispersed on the whole surface including both {001} and {10} facets of R-TiO_2-001 samples. It is reasonable for this phenomenon because the defective Ti^{3+} sites are uniformly exited without selectivity in the whole of bulk TiO_2. Correspondingly, the in-situ reduction of Pt^{4+} to Pt^0 or other valence states by defective Ti^{3+} sites is also dispersed uniformly without selectivity (both on {001} and {101} facets). Loading metallic Pt on the surface of TiO_2 has often been employed as a co-catalyst to separate the photoinduced charge carriers. Moreover, the loaded Pt, which acts as an active site, could catalyze H_2 evolution. Thus, the homogeneous distribution of ultrafine Pt on Ti^{3+}-doped faceted TiO_2 was found to be possibly effective for enhancing the photocatalytic H_2

DOI: 10.1021/acsomega.9b01648
ACS Omega 2019, 4, 14902−14912

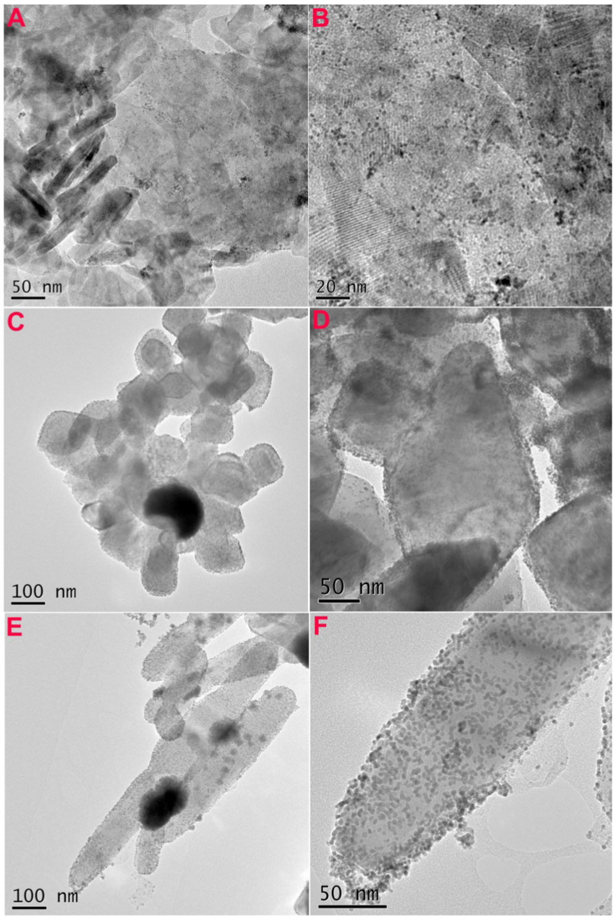

Figure 8. TEM images of platinum (Pt) nanoparticles loaded on (A, B) R-TiO_2-001; (C, D) R-TiO_2-101, and (E, F) R-TiO_2-100 samples by UV light irradiation.

production. Moreover, the ultrafine Pt particles were also dispersed uniformly without selectivity on the whole surface of R-TiO_2-101 and R-TiO_2-100 samples, as can be seen from Figure 8C−F, respectively.

Recycling and stability tests were evaluated by carrying out recycling reactions five times for the photocatalytic degradation of MO over R-TiO_2-001, R-TiO_2-101, and R-TiO_2-100, as shown in Figure 9. All of the Ti^{3+}-doped TiO_2 samples still retain good stability and durability after recycling 5 times,

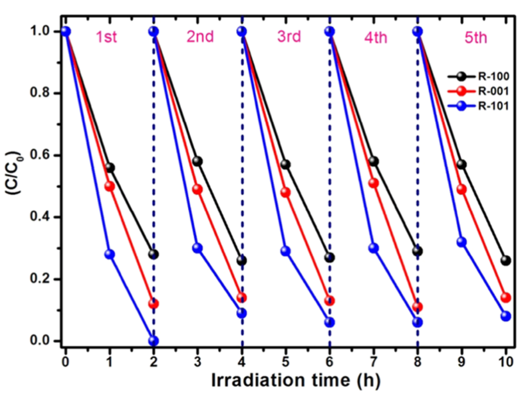

Figure 9. Stability tests of UV light irradiation-induced photocatalytic degradation of MO solution over the as-prepared Al reduced TiO_2 with different dominant exposed facets.

keeping a MO degradation order of R-TiO_2-101 > R-TiO_2-001 > R-TiO_2-100. To further address the recycling and stability issues, the XRD patterns and TEM images of Ti^{3+}-doped TiO_2 nanocrystals after photocatalytic activity tests were also provided, as is shown in Figures S9 and S10. All of the TiO_2 samples still retained a pure crystallized anatase phase and typical morphology (nanosheets for R-TiO_2-001, truncated bipyramids for R-TiO_2-101 and tetragonal faceted-nanorods for R-TiO_2-100), indicating excellent stability of the as-prepared TiO_2 samples.

Furthermore, to observe the effects of Ti^{3+} doping and exposed crystal facets toward the band structure of prepared TiO_2, the valence band (VB) X-ray photoelectron spectroscopy (XPS) are provided, as shown in Figure S11. Unexpectedly, all of the as-prepared TiO_2 samples display a typical VB characteristic of TiO_2, with an almost identical VB edge of the maximum energy for specified dominated exposed faceted TiO_2 before (Figure S11A) and after (Figure S11B) Ti^{3+} doping, which is similar to the reported defective titania.[42] However, the valence band maximum (VBM) among different dominant faceted TiO_2 shows a small distinction. More specifically, the VBM values for {001}, {101}, and {100} facets dominated TiO_2 before and after Ti^{3+} doping are 2.54, 2.56, and 2.53 eV, respectively. As for the photocatalytic process, photoexcitation, charge diffusion in bulk, and surface transfer of photoexcited electron and holes are the three key steps. Correspondingly, the photoreactivity is strongly depended on the comprehensive effects of absorbance, redox potential, and mobility of charge carriers, which are determined by electronic band structures as well as their surface atomic structure. Consequently, the photoreactivity of the prepared Ti^{3+}-doped TiO_2 crystals must be related to both its surface atomic structure and surface electronic band structure.

Accordingly, based on the UV−vis absorption and VB XPS spectra, electronic band structures of the as-prepared anatase TiO_2 crystals before and after Ti^{3+} doping were systematically investigated, as shown in Figure 10. Among these facets, the

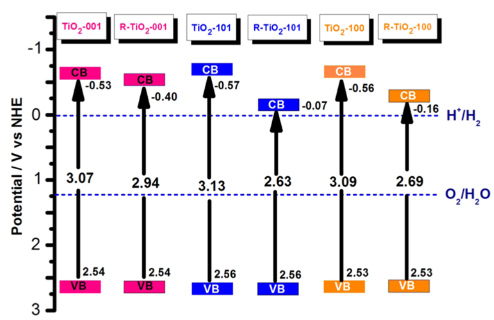

Figure 10. As obtained valence and conduction band edges of TiO_2 nanocrystals with dominated 001, 101, and 100 facets before and after Ti^{3+} doping.

{101} facet has the most positive CB position, and the {100} facet before Ti^{3+} doping has the most negative VB position. After Ti^{3+} doping, the CB position exhibits a downward shift tendency while keeping the VB position identical to that of non-Ti^{3+} doped ones. Specifically, the CB position order is doped {101} facet > doped {100} facet > doped {001} facet > {001} facet > {100} facet > {101} facet, and the VB position order is {100} facet ≈ doped {100} facet < {001} facet ≈ doped {001} facet < {101} facet ≈ doped {101} facet. Thus, a {001}/{101} binary facet junction can be formed in TiO_2 with

DOI: 10.1021/acsomega.9b01648
ACS Omega 2019, 4, 14902−14912

predominant exposed {001} and {101} facet, and a {001}/{101}/{100} ternary facet junction can be also formed. The resulting facet heterojunction is responsible for the transport and separation of charge carriers, together with the variable facet energy level, making the photocatalytic activity of TiO_2 with respectively predominated exposed facets to differ considerably.

The photoluminescence (PL) spectra of the prepared TiO_2 samples excited at 320 nm are shown in Figure 11. The profiles of the emission spectra are almost similar in which two main emission peaks at 397 and 427 nm appeared. The first one is attributed to the emission of the band−band PL process of anatase, while the latter is attributed to the excitonic PL process at the band edge.[43] As for pristine TiO_2, the PL intensity shows an order of TiO_2-001 < TiO_2-101 < TiO_2-100, further highlighting the key role of exposed facets in modulating the charge carriers. However, after Ti^{3+} doping, the separation efficiency of photoinduced charge carriers is just distinct. More specifically, the observed PL peak intensity of both R-TiO_2-101 and R-TiO_2-100 is much lower than that of TiO_2-101 and TiO_2-100, indicating that certain amounts of Ti^{3+} doping is beneficial to reduce the recombination efficiency of electrons and holes, which generally favors high photocatalytic activity. However, R-TiO_2-001 shows the higher PL intensity in both of the band−band and excitonic PL signals, indicating the higher recombination rates of photoinduced charge carriers. This is because the high concentration of Ti^{3+} forms new trapping centers of photoinduced carriers, which is unfavorable to the separation and transport of carriers and photocatalytic performance. To further understand the effects of Ti^{3+} and facets to the transport and separation of charge carriers for the prepared TiO_2 samples, transient fluorescence lifetime-based technique was further utilized. The fluorescence decay curves were further fitted using a biexponential function $I(t)$ based on a nonlinear least squares analysis using the following equation[44,45]

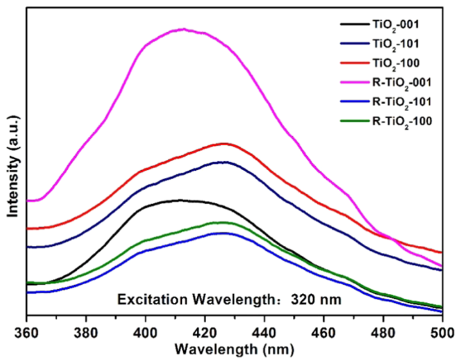

Figure 11. Photoluminescence spectrum of the as-prepared TiO_2 samples with dominated exposed {001}, {101}, and {100} facets before and after Al reduction.

$$I(t) = A_1 \exp\left(-\frac{t}{\tau_1}\right) + A_2 \exp\left(-\frac{t}{\tau_2}\right)$$

where τ_1 and τ_2 represent the decay time constants and A_1 and A_2 are the fractional contributions of the time-resolved decay time of τ_1 and τ_2, respectively. The average lifetime (τ_{avg}) of the as-prepared TiO_2 samples was calculated using the following equation

$$\tau_{avg} = \frac{A_1\tau_1^{\ 2} + A_2\tau_2^{\ 2}}{A_1\tau_1 + A_2\tau_2}$$

To obtain a clear overview of the fluorescence lifetime difference among TiO_2 samples with predominant exposed facets before and after Ti^{3+} doping, the lifetime of charge carriers measured by time-resolved fluorescence decay spectra (shown in Figure S12). The fitted fluorescence lifetime of TiO_2 results is summarized in Table 2. As for TiO_2 with dominated exposed {001}, {101}, and {100} faceted samples before Ti^{3+} doping, the average lifetime was 8.748, 6.290, and 5.767 ns, respectively. After Ti^{3+} doping, the average lifetime for R-TiO_2-101 and R-TiO_2-100 were significantly increased, corresponding to 10.058 and 7.784 ns, respectively. However, the R-TiO_2-001 exhibited a relatively lower average lifetime of 5.695 ns, further verifying that too much Ti^{3+} trapping sites inevitably increased the recombination rates of charge carriers and shortened the lifetime of photogenerated electrons and holes.

Based on the above results, we can now highlight the true determining factors of photoreactivity of Ti^{3+}-doped TiO_2 nanocrystals with respectively dominant exposed {001}, {101}, and {100} facets. First, exposure of anisotropic predominant crystal facets endows different density of low-coordinated atoms, which always serve as reactive photocatalytic sites. Second, the prepared binary faceted system by {001}/{101} for TiO_2 with dominant exposed {001} or {101} facets and ternary faceted junction by {001}/{101}/{100} for TiO_2 with dominant exposed {100} facets may provide a

Table 2. Fitted Fluorescence Lifetime of TiO_2 Samples with Predominant Exposed {001}, {101}, and {100} Facets before and after Ti^{3+} Doping

sample	lifetime ⟨τ⟩, ns	A %	average lifetime ⟨τ_{avg}⟩, ns	χ^2
TiO_2-001	τ_1 = 9.092	A_1 = 73.56	8.748	0.99390
	τ_2 = 1.145	A_2 = 26.44		
TiO_2-101	τ_1 = 1.091	A_1 = 70.18	6.290	0.99452
	τ_2 = 8.303	A_2 = 23.82		
TiO_2-100	τ_1 = 1.104	A_1 = 73.72	5.767	0.99504
	τ_2 = 8.508	A_2 = 16.28		
R-TiO_2-001	τ_1 = 1.031	A_1 = 64.41	5.695	0.99438
	τ_2 = 6.947	A_2 = 35.59		
R-TiO_2-101	τ_1 = 10.384	A_1 = 74.79	10.058	0.99338
	τ_2 = 1.125	A_2 = 25.21		
R-TiO_2-100	τ_1 = 1.190	A_1 = 70	7.784	0.99369
	τ_2 = 9.674	A_2 = 30		

DOI: 10.1021/acsomega.9b01648
ACS Omega 2019, 4, 14902−14912

cascade path among two adjacent facets for the efficient transfer and flow of photoinduced electrons and holes with different photoreduction and oxidation capacity. Third, the defective Ti^{3+} energy level may strongly be affected by the pristine electronic band structure of TiO_2 exposed with dominant {001}, {101}, and {100} facets, which finally provide different driving forces for the photoexcited e^- and h^+ and average lifetime of photoinduced charge carriers.

■ CONCLUSIONS

We have demonstrated that Ti^{3+} doping with respectively dominated exposed {001}, {101}, and {100} facets on anatase TiO_2 nanocrystals could favorably enhance the photocatalytic activity of degradation of MO and H_2 production under both UV and vis-light irradiation. The distinguished optical absorption differentiation is ascribed to the synergistic effects of both dominated crystal facet exposure and variable Ti^{3+} doping concentration. As for the photocatalytic H_2 production, R-TiO_2-001 demonstrated a much higher UV and vis-light-induced performance than R-TiO_2-101 and R-TiO_2-100, showing an order of R-TiO_2-001 > R-TiO_2-101 > R-TiO_2-100, which is consistent with the order of nonreduced TiO_2. Moreover, the photocatalytic H_2 production under UV light for R-TiO_2-001, R-TiO_2-101, and R-TiO_2-100 increased by a factor of 1.34, 2.65, and 3.39, while a factor of 8.90, 13.47, and 8.72 was achieved under visible light. In comparison, the photocatalytic degradation performance of MO under UV light for R-TiO_2-001, R-TiO_2-101, and R-TiO_2-100 increased by a factor of 3.18, 1.42, and 2.17, while a factor of 4.03, 2.85, and 1.58 was achieved under vis-light. The possible reasons for the differential ability of photo-oxidation and photoreduction are the exposure of more active sites, newly formed Ti^{3+} energy state with variable doping levels to extend the visible light response, the facilitated charge carrier separation and transfer among {001}, {101}, and {100} facets. Hopefully, this work can provide significant insights into the photoreactivity effect of Ti^{3+}-doped anatase TiO_2 crystals with dominant exposed {001}, {101}, and {100} facets and make a contribution to designing more efficient and stable solar fuel photocatalysts.

■ MATERIALS AND METHODS

Materials. Titanium butoxide (Aladdin, ≥99.0%), hydrofluoric acid (Aladdin, ≥40%), Degussa P25, potassium hydroxide (KOH, AR), sodium hydroxide (NaOH, AR), and hexamethylenetetramine (AR). All chemical reagents were of analytical grade and used as received without further purification.

Synthesis. *Preparation of TiO_2-001.* TiO_2 nanosheets with dominated exposure of {001} facets were prepared by the hydrothermal method similar to the methods reported elsewhere.[46] Then, the obtained powder was treated in an electric muffle furnace at 500 °C in air for 5 h and denoted TiO_2-001.

Preparation of TiO_2-101. The preparation methods of TiO2 exposed with dominant {101} is used according to the literature method.[47] After that, the obtained powder was treated in an electric muffle furnace at 500 °C in air for 5 h and the prepared samples were denoted as TiO_2-101.

Preparation of TiO_2-100. TiO_2 nanocrystals with the predominated {100} facet were prepared by hydrothermal treatment of titanate nanotubes twice as reported elsewhere.[16] Then, the obtained powder was treated in an electric muffle furnace at 500 °C in air for 5 h and the as-prepared sample is denoted as TiO_2-100.

Preparation of Ti^{3+}-Doped TiO_2 with Dominant {001}, {101}, and {100} Facets. Ti^{3+}-doped TiO_2 nanocrystals were prepared by molten Al reduction according to the literature reported elsewhere. In detail, the Al powders and pristine TiO_2 were separately placed in an evacuated two-zone furnace and treated at 800 °C (molten Al) and 500 °C (TiO_2) for 5 h in a 5×10^{-4} Pa pressure. The as-reduced TiO_2 was denoted as R-TiO_2-001, R-TiO_2-101, and R-TiO_2-100, respectively.

Pt loading on Ti^{3+}-doped TiO_2. Photoreduction of the platinum (Pt) loading on Ti^{3+}-doped TiO_2 nanocrystals was performed in a 100 mL Pyrex flask containing 0.01 g of TiO_2 powder, 5 mL of methanol, 0.5 mL of H_2PtCl_6 aqueous solution (1 wt %), and 45 mL of water at room temperature. The photoreduction time was conducted on a 300 W mercury lamp for 0.5 h. After that, the powder was carefully collected and washed with ethanol and water three times for further analysis.

Characterization. The morphology of the samples was observed using a field-emission scanning electron microscope (FE-SEM; JSM-6701F, JEOL) operated at an accelerating voltage of 5.00 kV and equipped with an energy dispersive spectrometer. Transmission electron microscopy (TEM) analyses were conducted with a JEM-1200EX electron microscope using a 200 kV accelerating voltage. X-ray diffraction (XRD) measurements were performed on an X' pert PRO diffractometer using Cu Kα radiation at 40 KeV and 40 mA. The XRD patterns were recorded from 10 to 70° with a scanning rate of 0.067°/s. X-ray photoelectron spectroscopy (XPS) was performed using an ESCALAB250Xi photoelectron spectrometer with an Al Kα X-ray excitation source to analyze the elemental composition of the samples. Ultraviolet−visible (UV−vis) absorption spectra were collected using a Shimadzu UV-2550 spectrophotometer at room temperature. ESR measurements were carried out using a JES-FA200 spectrometer/X-bond under room temperature at an X-band frequency of 9219.77 MHz, sweep width of 500 mT, and center field of 500 mT. Nitrogen-adsorption/desorption isotherms were obtained on an ASAP 2020M (Micromeritics Instruments) nitrogen-adsorption apparatus. The fluorescence lifetimes of prepared TiO_2 were taken on a steady/transient fluorescence spectrometer (FLS-1000, Edinburgh Instruments) to detect the lifetime of charge carriers for the prepared samples. All of the samples were degassed at 80 °C prior to Brunauer−Emmett−Teller (BET) measurements. The BET-specific surface area (SBET) was determined by a multipoint BET method using the adsorption data within the relative pressure (P/P_0) range of 0.05−0.3. The desorption branches data were used to determine the pore-size distribution using the Barret−Joyner−Halender method. The nitrogen-adsorption volume at P/P_0 = 0.97 was used to determine the pore volume and average pore size.

Photocatalytic Activity Measurement. Photocatalytic hydrogen production: the photocatalytic H_2 production was examined in a Pyrex top-irradiation type reaction vessel connected to a closed gas circulation system. Typically, 0.1 g of catalyst, 90 mL of deionized water, 10 mL of absolute methanol (as the sacrificial reagents), and 0.5 mL of 1 wt % H_2PtCl_6 aqueous solution were mixed uniformly and subjected to ultrasonic treatment for 30 min. At the given time interval, gas chromatography (Agilent; GC-7890A, MS-5A column, TCD, Ar carrier) was used to analyze the evolved gases.

DOI: 10.1021/acsomega.9b01648
ACS Omega 2019, 4, 14902−14912

Photocatalytic degradation of methyl orange (MO): typically, 0.1 g of TiO_2 sample and 100 mL of 20 mg/L MO aqueous solution were mixed and subjected to ultrasonic treatment sufficiently. After that, the suspension was magnetically stirred in the dark for 30 min to ensure that adsorption−desorption equilibrium was achieved. After light irradiation, the concentration change of MO was monitored using a UV−vis spectrometer at 464 nm. As for reusability, the photocatalyst was filtered and dried thoroughly after each cycle, and then the fresh MO solution was added for further analysis. In the case of the phenol degradation (phenol content characterized by the absorbance peak at 270 nm), the experimental conditions are the same as the MO degradation except for the amounts of catalysts (0.05 g) and concentrations of phenol aqueous solution (50 mL, 10^{-4} mol/L).

■ ASSOCIATED CONTENT

Supporting Information

The Supporting Information is available free of charge on the ACS Publications website at DOI: 10.1021/acsomega.9b01648.

> SEM images of pristine undoped TiO_2; schematic of the atomic surface structure of anatase TiO_2; XPS spectra of Ti, F, and Al elements and VB spectra; N_2 adsorption/desorption isotherm, pore volume and BET-specific surface area; digital photograph of prepared TiO_2; photocatalytic degradation of phenol; XRD patterns and TEM images of TiO_2 samples after evaluation of photoreactivity; time-resolved fluorescence decay spectra (PDF)

■ AUTHOR INFORMATION

Corresponding Author

*E-mail: lxg133298@163.com.

ORCID

Xiaogang Liu: 0000-0002-2063-1956

Author Contributions

This manuscript was written through contributions of all authors. All authors have given approval to the final version of the manuscript.

Notes

The authors declare no competing financial interest.

■ ACKNOWLEDGMENTS

This study was supported by the National Natural Science Foundation of China (21902140) and the Henan Provincial Science and Technology Research Projects (192102210005) and the Nanhu Scholars Program for Young Scholars of XYNU.

■ REFERENCES

(1) Fujishima, A.; Honda, K. Electrochemical Photolysis of Water at a Semiconductor Electrode. *Nature* **1972**, *238*, 37.

(2) Tada, H.; Fujishima, M.; Kobayashi, H. Photodeposition of Metal Sulfide Quantum Dots on Titanium (IV) Dioxide and the Applications to Solar Energy Conversion. *Chem. Soc. Rev.* **2011**, *40*, 4232−4243.

(3) Chen, H.; Nanayakkara, C. E.; Grassian, V. H. Titanium Dioxide Photocatalysis in Atmospheric Chemistry. *Chem. Rev.* **2012**, *112*, 5919−5948.

(4) Liu, X.; Dong, G.; Li, S.; Lu, G.; Bi, Y. Direct Observation of Charge Separation on Anatase TiO_2 Crystals with Selectively Etched {001} Facets. *J. Am. Chem. Soc.* **2016**, *138*, 2917−2920.

(5) Etgar, L.; Zhang, W.; Gabriel, S.; Hickey, S. G.; Nazeeruddin, M. K.; Eychmüller, A.; Liu, B.; Grätzel, M. High Efficiency Quantum Dot Heterojunction Solar Cell Using Anatase (001) TiO_2 Nanosheets. *Adv. Mater.* **2012**, *24*, 2202−2206.

(6) Li, X.; Zhao, Y.; Wang, X.; Wang, J.; Gaskov, A. M.; Akbar, S. Reduced Graphene Oxide (RGO) Decorated TiO_2 Microspheres for Selective Room-Temperature Gas Sensors. *Sens. Actuators, B* **2016**, *230*, 330−336.

(7) Zheng, Q.; Zhou, B.; Bai, J.; Li, L.; Jin, Z.; Zhang, J.; Li, J.; Liu, Y.; Cai, W.; Zhu, X. Self-Organized TiO_2 Nanotube Array Sensor for the Determination of Chemical Oxygen Demand. *Adv. Mater.* **2008**, *20*, 1044−1049.

(8) Sułek, A.; Pucelik, B.; Kuncewicz, J.; Dubin, G.; Dąbrowski, J. M. Sensitization of TiO_2 by Halogenated Porphyrin Derivatives for Visible Light Biomedical and Environmental Photocatalysis. *Catal. Today* **2019**, 538−549.

(9) Sugita, Y.; Ishizaki, K.; Iwasa, F.; Ueno, T.; Minamikawa, H.; Yamada, M.; Suzuki, T.; Ogawa, T. Effects of Pico-to-Nanometer-Thin TiO_2 Coating on the Biological Properties of Microroughened Titanium. *Biomaterials* **2011**, *32*, 8374−8384.

(10) Liu, G.; Yang, H. G.; Pan, J.; Yang, Y. Q.; Lu, G. Q.; Cheng, H.-M. Titanium Dioxide Crystals with Tailored Facets. *Chem. Rev.* **2014**, *114*, 9559−9612.

(11) Lazzeri, M.; Vittadini, A.; Selloni, A. Structure and Energetics of Stoichiometric TiO_2 Anatase Surfaces. *Phys. Rev. B* **2001**, *63*, No. 155409.

(12) Ray, C.; Pal, T. Recent Advances of Metal-Metal Oxide Nanocomposites and Their Tailored Nanostructures in Numerous Catalytic Applications. *J. Mater. Chem. A* **2017**, *5*, 9465−9487.

(13) Shen, S.; Chen, J.; Wang, M.; Sheng, X.; Chen, X.; Feng, X.; Mao, S. S. Titanium Dioxide Nanostructures for Photoelectrochemical Applications. *Prog. Mater. Sci.* **2018**, *98*, 299−385.

(14) Yang, H. G.; Sun, C. H.; Qiao, S. Z.; Zou, J.; Liu, G.; Smith, S. C.; Cheng, H. M.; Lu, G. Q. Anatase TiO_2 Single Crystals with a Large Percentage of Reactive Facets. *Nature* **2008**, *453*, 638.

(15) Zhao, X.; Jin, W.; Cai, J.; Ye, J.; Li, Z.; Ma, Y.; Xie, J.; Qi, L. Shape-and Size-Controlled Synthesis of Uniform Anatase TiO_2 Nanocuboids Enclosed by Active {100} and {001} Facets. *Adv. Funct. Mater.* **2011**, *21*, 3554−3563.

(16) Li, J.; Xu, D. Tetragonal Faceted-Nanorods of Anatase TiO_2 Single Crystals with a Large Percentage of Active {100} Facets. *Chem. Commun.* **2010**, *46*, 2301−2303.

(17) Xu, H.; Ouyang, S.; Li, P.; Kako, T.; Ye, J. High-Active Anatase TiO_2 Nanosheets Exposed with 95%{100} Facets toward Efficient H_2 Evolution and CO_2 Photoreduction. *ACS Appl. Mater. Interfaces* **2013**, *5*, 1348−1354.

(18) Barnard, A.; Curtiss, L. Prediction of TiO_2 Nanoparticle Phase and Shape Transitions Controlled by Surface Chemistry. *Nano Lett.* **2005**, *5*, 1261−1266.

(19) Pan, J.; Liu, G.; Lu, G. Q.; Cheng, H. M. On the True Photoreactivity Order of {001},{010}, and {101} Facets of Anatase TiO_2 Crystals. *Angew. Chem., Int. Ed.* **2011**, *50*, 2133−2137.

(20) Zhao, Z.; Li, Z.; Zou, Z. Surface Properties and Electronic Structure of Low-Index Stoichiometric Anatase TiO_2 Surfaces. *J. Phys.: Condens. Matter* **2010**, *22*, No. 175008.

(21) Chen, Y.; Li, W.; Wang, J.; Gan, Y.; Liu, L.; Ju, M. Microwave-Assisted Ionic Liquid Synthesis of Ti^{3+} Self-Doped TiO_2 Hollow Nanocrystals with Enhanced Visible-Light Photoactivity. *Appl. Catal., B* **2016**, *191*, 94−105.

(22) Chen, J.; Song, W.; Hou, H.; Zhang, Y.; Jing, M.; Jia, X.; Ji, X. Ti^{3+} Self-Doped Dark Rutile TiO_2 Ultrafine Nanorods with Durable High-Rate Capability for Lithium-Ion Batteries. *Adv. Funct. Mater.* **2015**, *25*, 6793−6801.

(23) Huang, Y.; Wang, P.; Wang, Z.; Rao, Y.; Cao, J.-j.; Pu, S.; Ho, W.; Lee, S. C. Protonated g-C_3N_4/Ti^{3+} Self-Doped TiO_2 Nanocomposite Films: Room-Temperature Preparation, Hydrophilicity,

and Application for Photocatalytic Nox Removal. *Appl. Catal., B* **2019**, *240*, 122−131.
(24) Fang, W.; Zhou, Y.; Dong, C.; Xing, M.; Zhang, J. Enhanced Photocatalytic Activities of Vacuum Activated TiO_2 Catalysts with Ti^{3+} and N Co-Doped. *Catal. Today* **2016**, *266*, 188−196.
(25) Xing, M.; Zhou, Y.; Dong, C.; Cai, L.; Zeng, L.; Shen, B.; Pan, L.; Dong, C.; Chai, Y.; Zhang, J.; Yin, Y. Modulation of the Reduction Potential of TiO_{2-X} by Fluorination for Efficient and Selective CH_4 Generation from CO_2 Photoreduction. *Nano Lett.* **2018**, *18*, 3384−3390.
(26) Naldoni, A.; Allieta, M.; Santangelo, S.; Marelli, M.; Fabbri, F.; Cappelli, S.; Bianchi, C. L.; Psaro, R.; Dal Santo, V. Effect of Nature and Location of Defects on Bandgap Narrowing in Black TiO_2 Nanoparticles. *J. Am. Chem. Soc.* **2012**, *134*, 7600−7603.
(27) Liu, B.; Zhao, X.; Yu, J.; Parkin, I. P.; Fujishima, A.; Nakata, K. Intrinsic Intermediate Gap States of TiO_2 Materials and Their Roles in Charge Carrier Kinetics. *J. Photochem. Photobiol., C* **2019**, 1−57.
(28) Zuo, F.; Wang, L.; Wu, T.; Zhang, Z.; Borchardt, D.; Feng, P. Self-Doped Ti^{3+} Enhanced Photocatalyst for Hydrogen Production under Visible Light. *J. Am. Chem. Soc.* **2010**, *132*, 11856−11857.
(29) Zhen, D.; Gao, C.; Yang, D.; Zhu, X.; Grimes, C. A.; Liu, Y.; Cai, Q. Blue Ti^{3+} Self-Doped TiO_2 Nanosheets with Rich {001} Facets for Photocatalytic Performance. *New J. Chem.* **2019**, *43*, 5759−5765.
(30) Liu, L.; Jiang, Y.; Zhao, H.; Chen, J.; Cheng, J.; Yang, K.; Li, Y. Engineering Coexposed {001} and {101} Facets in Oxygen-Deficient TiO_2 Nanocrystals for Enhanced CO_2 Photoreduction under Visible Light. *ACS Catal.* **2016**, *6*, 1097−1108.
(31) Amano, F.; Yasumoto, T.; Prieto-Mahaney, O.-O.; Uchida, S.; Shibayama, T.; Ohtani, B. Photocatalytic Activity of Octahedral Single-Crystalline Mesoparticles of Anatase Titanium (IV) Oxide. *Chem. Commun.* **2009**, 2311−2313.
(32) Hengerer, R.; Kavan, L.; Krtil, P.; Grätzel, M. Orientation Dependence of Charge-Transfer Processes on TiO_2 (Anatase) Single Crystals. *J. Electrochem. Soc.* **2000**, *147*, 1467−1472.
(33) Kavan, L.; Grätzel, M.; Gilbert, S.; Klemenz, C.; Scheel, H. Electrochemical and Photoelectrochemical Investigation of Single-Crystal Anatase. *J. Am. Chem. Soc.* **1996**, *118*, 6716−6723.
(34) Yan, Y.; Han, M.; Konkin, A.; Koppe, T.; Wang, D.; Andreu, T.; Chen, G.; Vetter, U.; Morante, J. R.; Schaaf, P. Slightly Hydrogenated TiO_2 with Enhanced Photocatalytic Performance. *J. Mater. Chem. A* **2014**, *2*, 12708−12716.
(35) Khan, M. M.; Ansari, S. A.; Pradhan, D.; Ansari, M. O.; Lee, J.; Cho, M. H.; Han, D. H. Band Gap Engineered TiO_2 Nanoparticles for Visible Light Induced Photoelectrochemical and Photocatalytic Studies. *J. Mater. Chem. A* **2014**, *2*, 637−644.
(36) Serwicka, E.; Schlierkamp, M.; Schindler, R. Localization of Conduction Band Electrons in Polycrystalline TiO_2 Studied by Esr. *Z. Naturforsch. A* **1981**, *36*, 226−232.
(37) Liu, X.; Bi, Y. Synergistic Effect of Ti^{3+} Doping and Facet Regulation over Ti^{3+}-Doped TiO_2 Nanosheets with Enhanced Photoreactivity. *Catal. Sci. Technol.* **2018**, *8*, 3876−3882.
(38) Zuo, F.; Bozhilov, K.; Dillon, R. J.; Wang, L.; Smith, P.; Zhao, X.; Bardeen, C.; Feng, P. Active Facets on Titanium (III)-Doped TiO_2: An Effective Strategy to Improve the Visible-Light Photocatalytic Activity. *Angew. Chem., Int. Ed.* **2012**, *51*, 6223−6226.
(39) Xiong, L.-B.; Li, J.-L.; Yang, B.; Yu, Y. Ti^{3+} in the Surface of Titanium Dioxide: Generation, Properties and Photocatalytic Application. *J. Nanomater.* **2012**, *2012*, 9.
(40) Zhu, Q.; Peng, Y.; Lin, L.; Fan, C.-M.; Gao, G.-Q.; Wang, R.-X.; Xu, A.-W. Stable Blue TiO_{2-X} Nanoparticles for Efficient Visible Light Photocatalysts. *J. Mater. Chem. A* **2014**, *2*, 4429−4437.
(41) Di Valentin, C.; Pacchioni, G.; Selloni, A. Reduced and N-Type Doped TiO_2: Nature of Ti^{3+} Species. *J. Phys. Chem. C* **2009**, *113*, 20543−20552.
(42) Wang, Z.; Yang, C.; Lin, T.; Yin, H.; Chen, P.; Wan, D.; Xu, F.; Huang, F.; Lin, J.; Xie, X.; Jiang, M. Visible-Light Photocatalytic, Solar Thermal and Photoelectrochemical Properties of Aluminium-Reduced Black Titania. *Energy Environ. Sci.* **2013**, *6*, 3007−3014.
(43) Liqiang, J.; Yichun, Q.; Baiqi, W.; Shudan, L.; Baojiang, J.; Libin, Y.; Wei, F.; Honggang, F.; Jiazhong, S. Review of Photoluminescence Performance of Nano-Sized Semiconductor Materials and Its Relationships with Photocatalytic Activity. *Sol. Energy Mater. Sol. Cells* **2006**, *90*, 1773−1787.
(44) Furube, A.; Asahi, T.; Masuhara, H.; Yamashita, H.; Anpo, M. Charge Carrier Dynamics of Standard TiO_2 Catalysts Revealed by Femtosecond Diffuse Reflectance Spectroscopy. *J. Phys. Chem. B* **1999**, *103*, 3120−3127.
(45) Li, Z.; Tian, B.; Zhang, W.; Zhang, X.; Wu, Y.; Lu, G. Enhancing Photoactivity for Hydrogen Generation by Electron Tunneling Via Flip-Flop Hopping over Iodinated Graphitic Carbon Nitride. *Appl. Catal., B* **2017**, *204*, 33−42.
(46) Yu, J.; Low, J.; Xiao, W.; Zhou, P.; Jaroniec, M. Enhanced Photocatalytic CO_2-Reduction Activity of Anatase TiO_2 by Coexposed {001} and {101} Facets. *J. Am. Chem. Soc.* **2014**, *136*, 8839−8842.
(47) Liu, C.; Han, X.; Xie, S.; Kuang, Q.; Wang, X.; Jin, M.; Xie, Z.; Zheng, L. Enhancing the Photocatalytic Activity of Anatase TiO_2 by Improving the Specific Facet-Induced Spontaneous Separation of Photogenerated Electrons and Holes. *Chem. - Asian J.* **2013**, *8*, 282−289.

DOI: 10.1021/acsomega.9b01648
ACS Omega 2019, 4, 14902−14912